



HAL
open science

Elbow dimensions in quadrupedal mammals driven by lubrication regime

Kalenia Marquez-Florez, Santiago Arroyave-Tobón, Loïc Tadrict, Jean-Marc Linares

► **To cite this version:**

Kalenia Marquez-Florez, Santiago Arroyave-Tobón, Loïc Tadrict, Jean-Marc Linares. Elbow dimensions in quadrupedal mammals driven by lubrication regime. *Scientific Reports*, 2024, 14 (1), pp.2177. 10.1038/s41598-023-50619-x . hal-04425079

HAL Id: hal-04425079

<https://hal.science/hal-04425079v1>

Submitted on 26 Jun 2024

HAL is a multi-disciplinary open access archive for the deposit and dissemination of scientific research documents, whether they are published or not. The documents may come from teaching and research institutions in France or abroad, or from public or private research centers.

L'archive ouverte pluridisciplinaire **HAL**, est destinée au dépôt et à la diffusion de documents scientifiques de niveau recherche, publiés ou non, émanant des établissements d'enseignement et de recherche français ou étrangers, des laboratoires publics ou privés.



OPEN

Elbow dimensions in quadrupedal mammals driven by lubrication regime

Kalenia Marquez-Florez , Santiago Arroyave-Tobon, Loïc Tadríst & Jean-Marc Linares

Synovial joints, such as the elbow, experience different lubrication regimes, ranging from fluid film to boundary lubrication, depending on locomotion conditions. We explore the relationship between the elbow lubrication regime and the size of quadrupedal mammals. We use allometry to analyze the dimensions, contact stress, and sliding speed of the elbow in 110 quadrupedal mammals. Our results reveal that the average diameter and width of the distal humerus are scaled $\propto M^{0.35}$, which allowed us to estimate a consistent contact pressure and sliding speed across mammals. This consistency likely promotes fluid film lubrication regardless of body mass. Further, the ratio between the diameter and width is about 0.5 for all analyzed taxa, which is a good compromise between loading capacity and size. Our study deepens our understanding of synovial joints and their adaptations, with implications for the development of treatments, prostheses, and bioinspired joint designs.

Synovial joints allow for relative movement of connected bones and fulfill weight-bearing functions. They collectively contribute to animal movement while minimizing energy loss due to friction¹. This low friction is attributed to the lubrication system of the joint, which limits tissue damage. Any breakdown of the components involved in the joint lubrication is associated with joint disorders and pathologies^{2,3}.

Understanding lubrication in synovial joints requires an extension of the principles of tribology, an engineering discipline that examines interactions between surfaces in relative motion. In general terms, lubrication conditions fall under various regimes, ranging from boundary to fluid film lubrication. In the fluid film regime, the conditions allow for a lubricant film between the interacting surfaces, preventing contact between asperities. This mechanism prevents friction and wear, in contrast to the boundary regime^{4,5}. The lubrication regime experienced by a joint is influenced by various variables: fluid and material variables (synovial fluid viscosity and cartilage material properties, which are consistent across taxa^{6–8}), and operational variables (applied normal load distributed in the joint, and the relative speed between the interacting surfaces, i.e., average contact stress and sliding speed). These operational variables, in turn, are conditioned by geometrical variables (dimensions of the interacting surfaces representing the joint), which are linked to animal size.

Over decades, researchers have extensively investigated synovial joint lubrication from both theoretical^{1,4,9–18}, and experimental^{2,3,19,20} perspectives, focusing in humans and specific animals species. However, the existing literature still presents challenges in inferring the relationship between geometrical and operational variables regarding lubrication behavior across taxa. For instance, are the lubrication conditions in a small mouse comparable to those in a large elephant? Understanding these relationships may pave the way for the development of innovative bioinspired mechanical joints and treatments for joint-related pathologies. The optimal synovial joint function should prioritize the fluid film lubrication regime, as it is known to reduce cartilage wear and tissue breakdown¹. If so, we hypothesize that joint dimensions adapted to the locomotion operational conditions favor the fluid–film lubrication regime. As fluid and material variables are both consistent across taxa, our hypothesis implies that joint dimensions should allow the sliding speed and average contact stress to also be consistent across taxa.

Here, we evaluate this hypothesis for the distal humerus in a sample of 110 quadrupedal mammals. This bone is crucial for locomotion^{21,22}, limb posture^{23,24}, and linked to ecological adaptations^{25–30}. Utilizing the dimensions of the distal humerus and the size of the animals, we estimate operational variables (i.e. sliding speed and average contact stress) during galloping. Among the different gaits of quadrupedal mammals, galloping induces the highest extension speeds of the elbow^{31–33}. We then extend the analysis to assess the lubrication regime, considering the estimated lubricant film thickness, for a simplified geometry of the elbow joint (modeled as cylinders in conformal contact, each with a layer of cartilage and an associated rugosity; see Fig. 1). Our analysis suggests that elbow dimensions consistently promote fluid film lubrication by maintaining consistent average contact

Aix Marseille Univ, CNRS, ISM, Marseille, France. ✉email: kalenia-maria.marquez-florez@univ-amu.fr

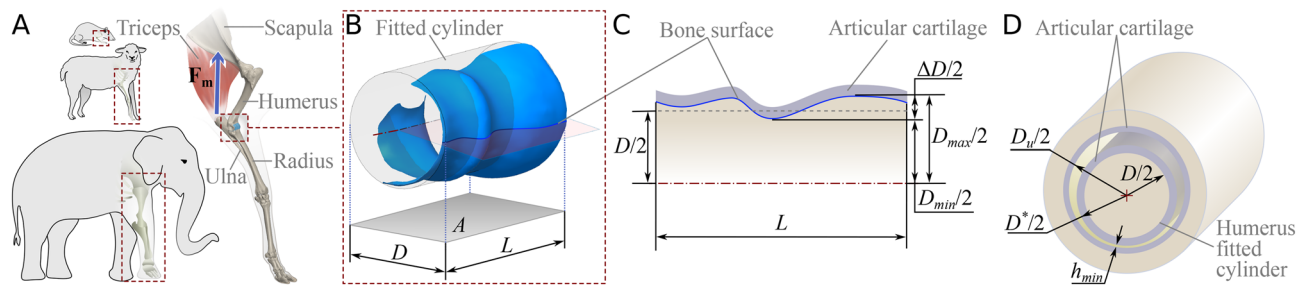


Figure 1. Analyzed dimensions on the distal humerus. **(A)** Forelimb of a *Ovis orientalis aries*. The triceps is represented with its resultant force, F_m . **(B)** Distal articular surface of the *Antelope cervicapra* humerus (object: MNHN:ZM:AC-1901-174, media ID: 000397840 from MorphoSource.org) with its fitted cylinder. The gray-colored region (with area A) is a projection of the fitted cylinder, along with the distal humerus average diameter, D , and width, L . **(C)** Profile of the distal humerus with the minimum diameter, D_{min} , maximum diameter, D_{max} , diameter difference ($\Delta D/2$), and the average diameter D . **(D)** Elbow equivalent cylindrical surfaces in conformal contact, where D^* is the humerus diameter including the cartilage thickness, D_u the diameter of the opposing surface, and h_{min} the minimum synovial fluid film thickness during elbow extension. D_u and the cartilage thickness were assumed to be proportional to D , based on values reported for the ankle¹².

stress and sliding speed across quadrupedal mammals. Our study deepens our understanding of synovial joints and how they endure functional requirements.

Results

Allometry of the distal humerus dimensions

The analyzed animals ranged from 0.02 kg to 4000 kg, (see Fig. 2 and SI-Table S2). The measured average diameter, D , of the distal humerus, ranged from 0.87 mm to 98.55 mm, and the width of the distal humerus, L , ranged from 2.1 mm to 164.9 mm (Table S1). Figure 1 shows the dimensions considered in this study.

We used phylogenetic generalized least squares (PGLS) analyzes to find the correlations of D and L with body mass, M : $D \propto M^{0.35}$ and $L \propto M^{0.35}$ (Fig. 3A and B). Interestingly, the ratio between D and L was found to be independent of the body mass, with $D/L \approx 0.5$ (confidence interval (ci): (0.4, 0.8)). The results indicated a strong correlation between these variables, where body mass explains 94% ($P < .001$) of the variations with a strong influence of the phylogenetic history (D : $\lambda = 0.78$; L : $\lambda = 0.79$; see Table S4).

We evaluated the ratio of the change in the radius, $\Delta D/2$ (Fig. 1), to the width of the distal humerus joint, L , to estimate the aspect ratio of the morphology of the articular surface profile: $\Delta D/2L$. The PGLS analysis showed no correlation between this ratio and body mass with a strong phylogenetic signal ($r^2 = 0.002$, $P = .638$, $\lambda = 0.93$), and gives a small allometric slope of -0.01 , suggesting independence of this ratio from body mass (Fig. 3C).

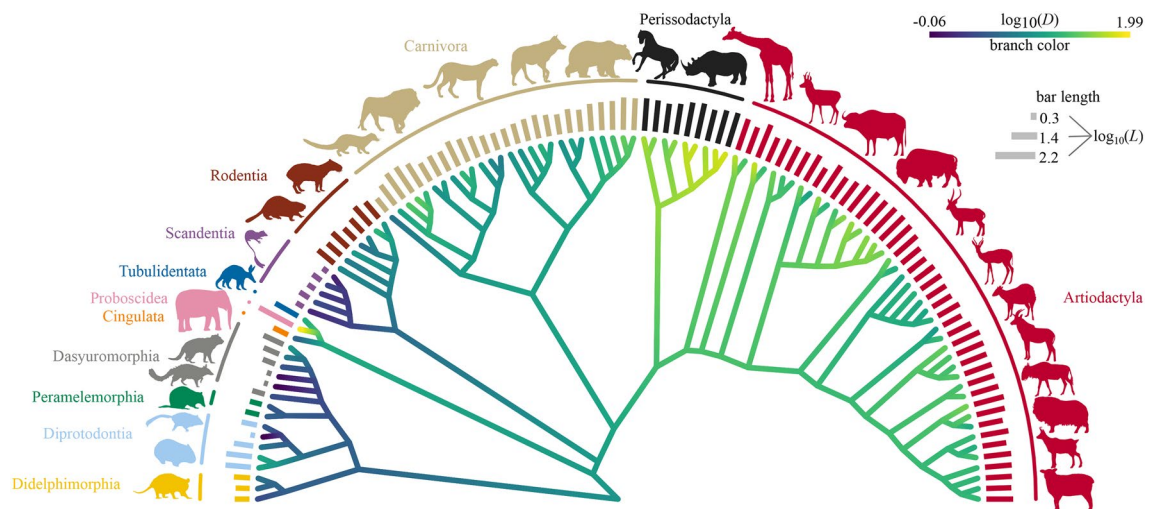


Figure 2. Phylogenetic tree with an overview of the taxa examined in the study. Branches are color-coded based on the \log_{10} -transformed average diameter $\log_{10}(D)$, but values other than those at the tip of the branches are approximate and do not support any conclusions. The outer bars length indicates the \log_{10} -transformed width $\log_{10}(L)$. The image was produced using modified branch lengths to improve visualization (with the function `compute.brLen` from the 'ape' package for R³⁴ following Grafen's method with a power of 0.65). The tree was plotted with the 'phytools' package for R³⁵. Silhouettes from PhyloPic (see Supplementary Information (SI) for silhouette credits).

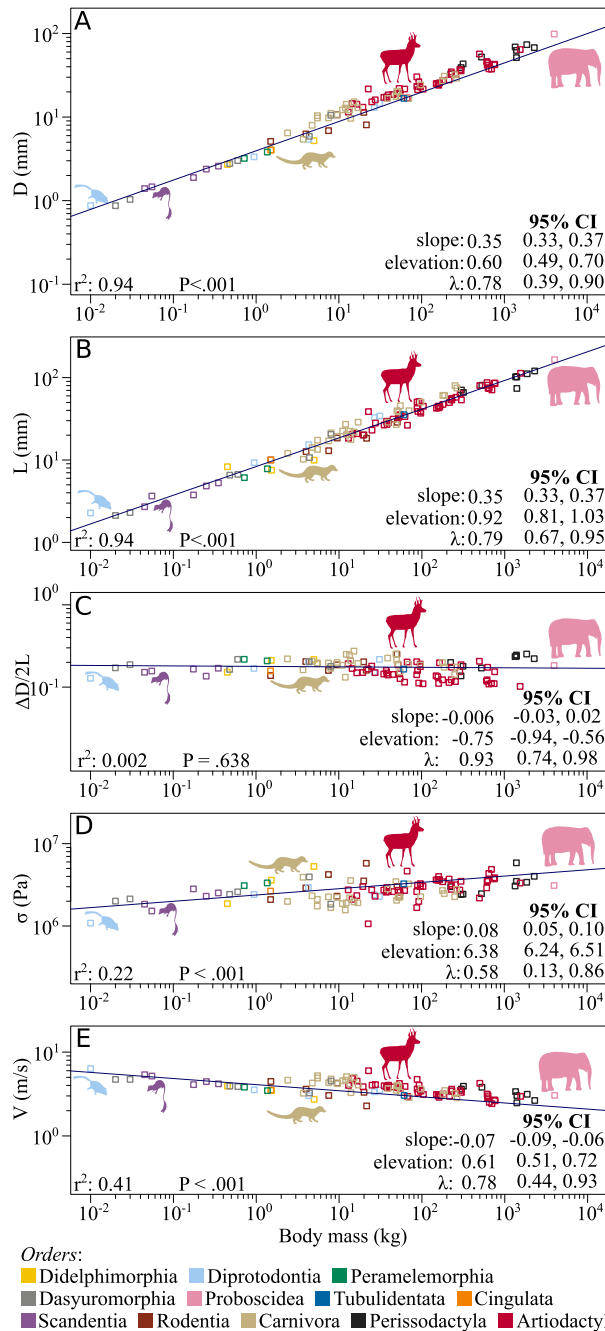


Figure 3. Allometry of analyzed parameters. (A) average diameter, D ; (B) width, L ; (C) ratio $\Delta D/2L$; (D) average contact stress, σ ; (E) sliding speed V . Slopes and elevations were estimated from phylogenetic generalized least squares (PGLS) regressions. The species (points) are color-coded according to their order. Silhouettes are from PhyloPic: *Acrobates pygmaeus* by Sarah Werning; CC BY 3.0; *Ptilocercus lowii*, Public Domain Dedication (PDD); *Genetta genetta*, Public Domain Mark 1.0; *Antilocapra americana*, PDD; *Elephas maximus*, PDD.

Estimated averaged contact stress σ

We defined σ as F_j/A , which is interpreted as the force at the joint, F_j , distributed uniformly on the area of the projection of the fitted cylinder: $A = LD$ (Fig. 1). We approximated F_j to the triceps concentric maximum force, F_m (see *asm4*). F_m was estimated as $A_m\sigma_m$, where A_m is the muscle cross-sectional area and σ_m the maximum stress the muscle can generate – consistent among vertebrates (about 0.2 – 0.3 MPa, here $\sigma_m = 0.25$ MPa)³⁶. A_m was estimated using the muscle mass, m_m , fiber length, L_m , and density, ρ_m : $A_m = m_m/(L_m\rho_m)$ ³⁶. In mammals, the triceps mass and fiber length allometries are $m_m = 6.2M^{1.11}$ (for the muscle mass in g and the body mass in kg) and $L_m = 18.7M^{0.33}$ (for fiber length in mm and the body mass in kg)³⁷. ρ_m is consistent among mammals at about 1060 kg/m³³⁷. From above, $F_m = 78.20M^{0.78}$ (for F_m in N and M in kg). Further, $\sigma \propto M^{0.08}$ (Fig. 3D),

thus, σ is consistent across all taxa, at about 2.4 ± 0.75 MPa. This is confirmed by the small correlation coefficient revealed by the PGLS regression ($r^2 = 0.23$, $P < .001$, $\lambda = 0.58$). For detailed statistics see Table S4.

Estimated maximum sliding speed V

We defined V as the relative speed at the joint average radius, $D/2$, during the rapid extension of the elbow; $V = \omega D/2$. The angular speed, ω , depends on the angular acceleration α and the joint excursion time, t , as $\omega = \alpha t$. The triceps force F_m (see *asm4*.) generates the acceleration, α , which is inversely proportional to the forearm's moment of inertia, I : $\alpha = F_m k/I$, where k is the moment arm of F_m . For the triceps, $k = 8.7 M^{0.41}$ (k in mm and the body mass in kg)³⁷. The moment of inertia at the elbow of the forearm scales as $I = 1.77 \times 10^{-5} M^{1.78}$ (I in kg m^2 and M in kg, see *asm6*. and SI-Fig. S3). The joint excursion time, t , is inversely proportional to the stride frequency, S_f : $t \propto S_f^{-1}$. For gallop, S_f is independent of speed and scales allometrically with body mass as $S_f = 4.70 M^{-0.16}$ (S_f in Hz and body mass in Kg)³⁸. According to *asm5*., t is a percentage of the stride period in galloping (specifically, 25.4% S_f^{-1} , see SI-Fig. S1). From above, $V \propto M^{-0.07}$ (Fig. 3E), thus, is consistent across all taxa, at about 4.1 ± 0.1 m/s. The PGLS revealed a weak correlation between V and body mass ($r^2 = 0.41$, $P < .001$, $\lambda = 0.78$). For detailed statistics see Table S4.

Estimated minimum lubricant film thickness h_{min}

In dynamically loaded joints, the lubrication mechanism is isoviscous-elastic, as cartilage deforms easily and the viscosity of synovial fluid varies little under physiological loads^{3,5,13,39}. Our modeling approach represents the elbow as two cylinders in conformal contact, each with diameters D^* and D_u (Fig. 1D). The modeling considers the presence of a layer of cartilage coating the cylinders, as well as the clearance between them (see Fig. 1D). Since we assume a constant cartilage thickness along the cylinders, D^* and D_u are functions of the average diameter, D , along with two proportionality parameters, c_i and c_{ii} , which define the articular cartilage thickness and the clearance, respectively (see SI-Fig. S7). Consequently, we express them as follows: $D^* = D(1 + c_i)$ and $D_u = D(1 + c_i + c_{ii})$. Based on measurements reported in the literature¹², we estimate that these values should be around $c_i = 0.06$ and $c_{ii} = 0.07$. However, due to the lack of sufficient information in the literature to estimate the values of c_i and c_{ii} , we conducted a sensitivity analysis to assess their impact on the lubricant film thickness (see SI-Fig. S8).

For tow cylinders in conformal contact, the minimum lubricant film thickness that separates the surfaces is given by $h_{min} = R_x(7.43U^{0.65}W^{-0.21})^5$. The effective radius, R_x , the dimensionless speed parameter U , and the dimensionless load parameter W , were estimated considering: $E = 8.1$ MPa⁶, $\nu = 0.47$, and $\eta = 0.01$ Pa·s⁸. R_x is defined as $R_x = D^*D_u/(2(D_u - D^*))$ (see Fig. 1); U as $\eta V^*/(E'R_x)$, where V^* is the sliding speed at D^* and E' is the effective Young's modulus: $E' = E/(1 - \nu)$. W is defined as $F_m/(E'R_x^2)$. These equations give $h_{min} \propto M^{0.06}$, independent of body mass, estimated at about 24 μm .

Discussion

We used allometry to analyze distal humerus dimensions, allowing us to estimate average contact stress, maximum sliding speed, and lubricant film thickness in 110 quadrupedal mammals. We estimated that the average contact stress and maximum sliding speed were consistent across taxa, aligning with the classical theories of allometry⁴⁰ (i.e. geometric similarity, elastic similarity, and constant stress similarity -see SI-Table S8). If so, this consistency allows for a constant minimum lubricant film thickness across taxa, ensuring a consistent lubrication regime. Therefore, a small mammal such as *Acrobates pygmaeus* (13 g) and a large one such as *Elephas maximus* (4000 kg) may experience similar lubrication conditions at the elbow during rapid extension of the joint.

The fact that joint fluid and material properties are similar across taxa⁶⁻⁸ suggests that joint dimensions likely evolved for tissue maintenance. This agrees with existing literature that highlights the adaptability of bone morphology to mechanical stimuli during development^{41,42}. Specifically, the consistent ratio $D/L \approx 0.5$ of the distal humerus strikes a balance between loading capacity and joint width. This ratio resembles industrial long bearings ($D/L \leq 0.5$), where lubricant film pressure varies little along the rotation axis, maximizing lubricant loading capacity and minimizing lubricant outflow⁴³.

The joint operational variables of maximum sliding speed and average contact stress were estimated consistent across taxa. Despite the simplification of the elbow as two cylinders, the sliding speed at a given point of the joint surface is consistent across taxa due to the constant aspect ratio of the joint profile ($\Delta D/2L$). The average contact stress, estimated at 2.4 MPa, falls within the range of intermittent compressive hydrostatic stress for chondrocytes to stay healthy (1 – 10 MPa)⁴⁴. Our findings align with those of Brand⁴⁵, who inferred from literature data of four mammal species that the average contact stress ranged from 0.1 – 2.9 MPa regardless of the joint.

Further, the quadrupedal mammal elbow might have adapted to attain fluid film lubrication under extreme locomotion, as in galloping. The estimated maximum sliding speed coupled with the estimated average contact stress promotes a minimum lubricant film thickness at about 24 μm for all analyzed taxa. In engineering, we use the film parameter Λ to characterize the lubrication regime. This parameter compares the minimum lubricant film thickness, h_{min} , to the combined roughness of the surfaces in contact, R_a : $\Lambda = h_{min}/\sqrt{2R_a}$ ⁵. In the traditional classification: $\Lambda < 1$ is boundary lubrication, $1 \leq \Lambda < 3$ is mixed lubrication and $\Lambda \geq 3$ is fluid film lubrication. As R_a for the articular cartilage has been measured at 1.42 μm ⁸, Λ is at about $12 \gg 3$. This suggests fluid film lubrication, with some security margin, which might ensure this lubrication during galloping even under conditions of high surface roughness (see SI-Figs. S9–S11). Additionally, local pressures can smooth out surface asperities, allowing fluid film lubrication even if $\Lambda < 1$ ^{44,46}. SI-Figure S9 details this modeling and evaluation of film thickness and lubrication regime while considering variations in the conformal contact hypothesis (i.e., changes in cartilage thickness and clearance between cylinders).

The findings of this study should be interpreted mindful of the assumptions. We estimated contact stress and sliding speed values based on measurements of distal humeri dimensions, coupled with allometric expressions from the literature, which may introduce potential uncertainties. Assumptions regarding the triceps force reaction time⁴⁷ and neglecting antagonist muscles^{31,47} may slightly affect the estimated maximum sliding speed. Hence, in SI-Figure S9 we further evaluated the combined effect of smaller sliding speeds and different roughnesses of the cartilage on the lubrication regime. While fluid film lubrication is maintained for small to moderate velocities and roughness, it shifts to mixed lubrication at very small sliding speeds (< 0.17 m/s) and to boundary lubrication for extremely low speeds (< 0.014 m/s). However, factors such as squeeze-film action and surface properties of the cartilage become significant at low speeds, which influence the lubrication regime⁸. Furthermore, our simplified model treated the elbow as two cylinders in contact, overlooking the complex morphology of the elbow. We also assumed an allometric similarity of cartilage thickness and joint clearance to the average diameter, potentially impacting the estimated lubrication regime. To assess the sensitivity of the regime to variations in cartilage thickness and joint clearance, we conducted a detailed analysis in SI-Figs. S8–S11. Additionally, while studies indicate a subperiosteal transmission of pressure⁴⁸, we opted to neglect this pressure due to its significant difference in magnitude compared to joint contact pressures, however, it might be considered in future works.

In conclusion, our study provides insight into the workings of natural joints. Our findings suggest that the dimensions of the distal humerus might have evolved so that stresses and sliding velocities promote fluid film lubrication, beneficial for tissue maintenance. This sizing strategy is similar to the bushing design in engineering, where dimensions rely on the ability of the material to withstand pressures and velocities. Ultimately, this study might eventually contribute to bioinspired joint designs.

Methods

Data collection

We obtained 3D-reconstructed humeri of quadrupedal extant mammals from the MorphoSource.org database. Only bones with ossified growth plates were considered for the analysis. Knuckle-walking mammals and primates were excluded due to differences in locomotion style and forelimb weight support during gait⁴⁹. Our dataset included 203 bones from 110 species across 35 families and 12 mammalian orders (SI-Table S1). We did not differentiate between the gender or lateral side of the bones. We searched published literature to obtain the average mass of the animals in the study (SI-Table S2).

Assumptions

We considered the following assumptions for the development of this study:

- asm1.* The distal humerus articular surface can be approximated as a revolution surface, and the elbow was simplified as two cylinders in conformal contact^{50,51}.
- asm2.* The variables are independent of each other if the magnitude of the allometric exponent is less than 0.1³⁸.
- asm3.* We analyzed the conditions of a rapid extension of the elbow which occurs naturally during galloping. In this gait, the stride frequency (S_f) only depends on the body mass³⁸.
- asm4.* In galloping (see *asm3.*), the triceps exhibits strong activity during elbow extension, surpassing the biceps and brachialis during flexion^{31–33}. The triceps uses elastic energy storage during locomotion to reduce the work done at the shoulder^{24,33,52}. Further, during galloping, muscles perform their maximal force which determines the ground reaction force and the loads on bones and joints⁵³. In that line, we assumed that: i) the triceps is in charge of the rapid extension of the elbow; ii) the force at the joint is similar to that of the triceps.
- asm5.* The duration of the extension periods was determined as a percentage of the stride using data from Tokuriki³¹ and the PlotDigitizer tool. On average, the extension instances make up 25.4% of the stride period (see SI-Fig. S1).
- asm6.* Using supplementary data from Coatham et al.⁵⁴ (who conducted virtual segmentation of computed tomography scans of animal skins), we calculated the moment of inertia, I , at the elbow of the lower arm (arm and hand) of quadrupedal mammals. We obtained $I = 1.77 \times 10^{-5} M^{1.78}$ (for I in kg m² and the mass in kg) (see SI-Fig S3).

Specimen measurements

We used the software 3D slicer⁵⁵ to place eight 3D anatomical landmarks, common to all specimens, and seven 3D semilandmarks at the edges of the distal humerus articular surface (they started and ended at anatomical landmarks⁵⁶) (SI-Fig. S5).

We used the 7 semilandmarks curves to extract a point cloud of the distal humerus articular surface. Then, we fitted a cylinder surface to the point cloud and determined the maximum diameter, D_{max} ; minimum diameter, D_{min} ; and the width, L , of the articular surface (SI-Fig. S6) (for the measurements of the distal humerus we developed a code in python published in <https://doi.org/10.5281/zenodo.7993776>). The radius of the fitted cylinder was defined as the average radius, D . As in previous studies, the measurements for species with multiple specimens were averaged^{57–59}.

Phylogenetic analysis

We used theoretical power-law relationships for scaling the parameters to body mass^{58,60}. $Y = aX^b$, where Y and X are the related parameters. By \log_{10} -transforming both sides, we obtain a linear function: $\log_{10}(Y) = \log_{10}(a) + b \log_{10}(X)$, where $\log_{10}(a)$ is the elevation of the line and b the slope.

We used phylogenetic generalized least-squares regressions (PGLS) to consider the impact of evolutionary relatedness on the data, using 10,000 phylogenetic trees obtained from the tool VertLife⁶¹. To quantify the extent to which the measurements were affected by evolutionary history, we estimated Pagel's λ by maximum likelihood optimization^{62,63}. All continuous variables were \log_{10} -transformed prior to the statistical analyses. We calculated allometries for all phylogenies and selected an average tree to serve as the representative tree (SI-Fig. S4). The 'ape' and 'caper' packages for R^{34,64,65} were used for the analyses.

We also used the standardized major axis (SMA) line-fitting method to examine the scaling relationships over the full range of body mass. While this approach does not consider phylogenetic relationships, provides a useful model for predicting patterns⁵⁸. Similar values for X often correspond to similar values for Y , but this does not necessarily indicate evolutionary relatedness⁶⁶. We used the 'smatr' package in R^{65,67,68}. The results are presented in SI-Table S5.

Data availability

The datasets generated and/or analysed during the current study are available in a Zenodo repository, <https://doi.org/10.5281/zenodo.7993776>.

Received: 18 July 2023; Accepted: 22 December 2023

Published online: 25 January 2024

References

- Popov, V. L., Poliakov, A. M. & Pakhaliuk, V. I. Synovial joints. Rriology, regeneration, regenerative rehabilitation and arthroplasty. *Lubricants* **9**, 15. <https://doi.org/10.3390/lubricants9020015> (2021).
- Lin, W. & Klein, J. Recent progress in cartilage lubrication. *Adv. Mater.* **33**, 2005513. <https://doi.org/10.1002/adma.202005513> (2021).
- Link, J. M., Salinas, E. Y., Hu, J. C. & Athanasiou, K. A. The tribology of cartilage: Mechanisms, experimental techniques, and relevance to translational tissue engineering. *Clin. Biomech.* **79**, 104880. <https://doi.org/10.1016/j.clinbiomech.2019.10.016> (2020).
- Jin, Z. M. & Dowson, D. Elastohydrodynamic lubrication in biological systems. *Proc. Inst. Mech. Eng. J. Tribol.* **219**, 367–380. <https://doi.org/10.1243/135065005X33982> (2005).
- Hamrock, B., Schmid, B. & Jacobson, B. *Fundamentals of Fluid Film Lubrication* (Mechanical engineering series (CRC Press, UK, 2004).
- Nieminen, M. T. *et al.* Prediction of biomechanical properties of articular cartilage with quantitative magnetic resonance imaging. *J. Biomech.* **37**, 321–328. [https://doi.org/10.1016/S0021-9290\(03\)00291-4](https://doi.org/10.1016/S0021-9290(03)00291-4) (2004).
- Kabir, W., Bella, C. D., Choong, P. F. & O'Connell, C. D. Assessment of native human articular cartilage: A biomechanical protocol. *Cartilage* **13**, 427S–437S. <https://doi.org/10.1177/1947603520973240> (2021).
- Liao, J., Smith, D. W., Miramini, S., Gardiner, B. S. & Zhang, L. Investigation of role of cartilage surface polymer brush border in lubrication of biological joints. *Friction* **10**, 110–127. <https://doi.org/10.1007/s40544-020-0468-y> (2022).
- Jones, E. S. Joint lubrication. *Lancet* **227**, 1043–1045. [https://doi.org/10.1016/S0140-6736\(01\)37157-X](https://doi.org/10.1016/S0140-6736(01)37157-X) (1936).
- Modes of lubrication in human joints. D., D. Paper 12. *Proceedings of the Institution of Mechanical Engineers, Conference Proceedings* **181**, 45–54. https://doi.org/10.1243/PIME_CONF_1966_181_206_02 (1966).
- Dowson, D., Unsworth, A. & Wright, V. Analysis of 'boosted lubrication' in human joints. *J. Mech. Eng. Sci.* **12**, 364–369. https://doi.org/10.1243/JMES_JOUR_1970_012_060_02 (1970).
- Medley, J. B., Dowson, D. & Wright, V. Surface geometry of the human ankle joint. *Eng. Med.* **12**, 35–41. https://doi.org/10.1243/EMED_JOUR_1983_012_008_02 (1983).
- Medley, J. B., Dowson, D. & Wright, V. Transient elastohydrodynamic lubrication models for the human ankle joint. *Eng. Med.* **13**, 137–151. https://doi.org/10.1243/EMED_JOUR_1984_013_035_02 (1984).
- Dowson, D. & Jin, Z.-M. Micro-elastohydrodynamic lubrication of synovial joints. *Eng. Med.* **15**, 63–65. https://doi.org/10.1243/EMED_JOUR_1986_015_019_02 (1986).
- Hou, J. S., Holmes, M. H., Lai, W. M. & Mow, V. C. Boundary conditions at the cartilage-synovial fluid interface for joint lubrication and theoretical verifications. *J. Biomech. Eng.* **111**, 78–87. <https://doi.org/10.1115/1.3168343> (1989).
- Jiang, M., Gao, L., Yang, P., Jin, Z. M. & Dowson, D. *Numerical Analysis of the Thermal Micro-EHL Problem of Point Contact with a Single Surface Bump* Vol. 48, 627–635 (Elsevier Masson SAS, 2005).
- Wang, Y., Chi Wong, D. W., Tan, Q., Li, Z. & Zhang, M. Total ankle arthroplasty and ankle arthrodesis affect the biomechanics of the inner foot differently. *Sci. Rep.* <https://doi.org/10.1038/s41598-019-50091-6> (2019).
- Al-Atawi, N. O. & Suleiman Mashat, D. Synovial joint study. *Am. J. Computat. Math.* **12**, 7–24. <https://doi.org/10.4236/ajcm.2022.121002> (2022).
- George, G. W. *et al.* Adaptive mechanically controlled lubrication mechanism found in articular joints. *Proc. Natl. Acad. Sci.* **108**, 5255–5259. <https://doi.org/10.1073/pnas.1101002108> (2011).
- Liao, J. *et al.* The investigation of fluid flow in cartilage contact gap. *J. Mech. Behav. Biomed. Mater.* **95**, 153–164. <https://doi.org/10.1016/j.jmbbm.2019.04.008> (2019).
- Susan G., L., Daniel, S., Pierre, L. & Mark, H. Uniqueness of primate forelimb posture during quadrupedal locomotion. *American Journal of Physical Anthropology* **112**, [https://doi.org/10.1002/\(sici\)1096-8644\(200005\)112:1%3C87::aid-ajpa9%3E3.0.co;2-b](https://doi.org/10.1002/(sici)1096-8644(200005)112:1%3C87::aid-ajpa9%3E3.0.co;2-b) (2000).
- Polly, P. D. Limbs in mammalian evolution. In *Fins into Limbs: Evolution, Development, and Transformation* Vol. 15 (ed. Hall, B. K.) 245–268 (University of Chicago Press, 2007).
- Shin-ichi, F. Olecranon orientation as an indicator of elbow joint angle in the stance phase, and estimation of forelimb posture in extinct quadruped animals. *J. Morphol.* **270**, 1107–1121. <https://doi.org/10.1002/jmor.10748> (2009).
- Fujiwara, S.-I. & Hutchinson, J. R. Elbow joint adductor moment arm as an indicator of forelimb posture in extinct quadrupedal tetrapods. *Proc. R. Soc. B Biol. Sci.* **279**, 2561–2570. <https://doi.org/10.1098/rspb.2012.0190> (2012).
- Andersson, K. Elbow-joint morphology as a guide to forearm function and foraging behaviour in mammalian carnivores. *Zool. J. Linn. Soc.* **142**, 91–104. <https://doi.org/10.1111/j.1096-3642.2004.00129.x> (2004).
- Borja, F., Alberto, M.-S. & Christine, M. Ecomorphological determinations in the absence of living analogues: The predatory behavior of the marsupial lion (thylacoleo carnifex) as revealed by elbow joint morphology. *Paleobiology* **42**, 508–531. <https://doi.org/10.1017/pab.2015.55> (2016).

27. Ruta, M., Krieger, J., Angelczyk, K. D. & Wills, M. A. The evolution of the tetrapod humerus: Morphometrics, disparity, and evolutionary rates. *Earth Environ. Sci. Trans. R. Soc. Edinb.* **109**, 351–369. <https://doi.org/10.1017/S1755691018000749> (2018).
28. Dickson, B. V., Clack, J. A., Smithson, T. R. & Pierce, S. E. Functional adaptive landscapes predict terrestrial capacity at the origin of limbs. *Nature* **589**, 242–245. <https://doi.org/10.1038/s41586-020-2974-5> (2021).
29. Hazel, L. & R., Peter J., B., David P., H., Justin W., A. & Alistair R., E., Low elbow mobility indicates unique forelimb posture and function in a giant extinct marsupial. *J. Anat.* **238**, 1425–1441. <https://doi.org/10.1111/joa.13389> (2021).
30. Billie, J., Alberto, M.-S., Emily, J. & R. & Christine M., J., Distal humeral morphology indicates locomotory divergence in extinct giant kangaroos. *J. Mammal. Evol.* **29**, 27–41. <https://doi.org/10.1007/s10914-021-09576-3> (2022).
31. Tokuriki, M. Electromyographic and joint-mechanical studies in quadrupedal locomotion : III. Gallop. *Jpn. J. Vet. Sci.* **36**, 121–132. <https://doi.org/10.1292/jvms1939.36.121> (1974).
32. English, A. W. An electromyographic analysis of forelimb muscles during overground stepping in the cat. *J. Exp. Biol.* **76**, 105–122. <https://doi.org/10.1242/jeb.76.1.105> (1978).
33. Carrier, D. R., Deban, S. M. & Fischbein, T. Locomotor function of forelimb protractor and retractor muscles of dogs: Evidence of strut-like behavior at the shoulder. *J. Exp. Biol.* **211**, 150–162. <https://doi.org/10.1242/jeb.010678> (2008).
34. Paradis, E. & Schliep, K. ape 5.0: An environment for modern phylogenetics and evolutionary analyses in R. *Bioinformatics* **35**, 526–528 (2019).
35. Revell, L. J. phytools: An R package for phylogenetic comparative biology (and other things). *Methods Ecol. Evol.* **3**, 217–223. <https://doi.org/10.1111/j.2041-210X.2011.00169.x> (2012).
36. Pollock, C. M. & Shadwick, R. E. Allometry of muscle, tendon, and elastic energy storage capacity in mammals. *Am. J. Physiol. Regul. Integr. Compar. Physiol.* <https://doi.org/10.1152/ajpregu.1994.266.3.r1022> (1994).
37. Alexander, R. M. N., Jayes, A. S., Maloiy, G. M. & Wathuta, E. M. Allometry of the leg muscles of mammals. *J. Zool.* **194**, 539–552. <https://doi.org/10.1111/j.1469-7998.1981.tb04600.x> (1981).
38. Heglund, N. C. & Taylor, C. R. Speed, stride frequency and energy cost per stride: How do they change with body size and gait?. *J. Exp. Biol.* **138**, 301–318. <https://doi.org/10.1242/jeb.138.1.301> (1988).
39. Dowson, D. & Yao, J. Paper IV (i) A full solution to the problem of film thickness prediction in natural synovial joints. In *Mechanics of Coatings*, vol. 17 of *Tribology Series*, 91–102, [https://doi.org/10.1016/S0167-8922\(08\)70245-1](https://doi.org/10.1016/S0167-8922(08)70245-1) (Elsevier, 1990).
40. McMahon, T. *Muscles, Reflexes, and Locomotion*. No. v. 10 in *Muscles, Reflexes, and Locomotion* (Princeton University Press, 1984).
41. Ng, J. L., Kersh, M. E., Kilbreath, S. & Tate, K. K. Establishing the basis for mechanobiology-based physical therapy protocols to potentiate cellular healing and tissue regeneration. *Front. Physiol.* **8**, 303. <https://doi.org/10.3389/fphys.2017.00303> (2017).
42. Carrera-Pinzón, A. F., Márquez-Flórez, K., Kraft, R. H., Ramtani, S. & Garzón-Alvarado, D. A. Computational model of a synovial joint morphogenesis. *Biomech. Model. Mechanobiol.* **19**, 1389–1402. <https://doi.org/10.1007/s10237-019-01277-4> (2020).
43. Hemmati, F., Miraskari, M. & Gadala, M. S. Dynamic analysis of short and long journal bearings in laminar and turbulent regimes, application in critical shaft stiffness determination. *Appl. Math. Model.* **48**, 451–475. <https://doi.org/10.1016/j.apm.2017.04.013> (2017).
44. Hamrick, M. W. A chondral modeling theory revisited. *J. Theor. Biol.* **201**, 201–208. <https://doi.org/10.1006/jtbi.1999.1025> (1999).
45. Brand, R. A. Joint contact stress: A reasonable surrogate for biological processes?. *Iowa Orthop. J.* **25**, 82–94 (2005).
46. Hansen, J., Björling, M. & Larsson, R. A new film parameter for rough surface EHL contacts with anisotropic and isotropic structures. *Tribol. Lett.* **69**, 37. <https://doi.org/10.1007/s11249-021-01411-3> (2021).
47. Khamoui, A. V. *et al.* Relationship between force-time and velocity-time characteristics of dynamic and isometric muscle actions. *J. Strength Cond. Res.* **25**, 198–204. <https://doi.org/10.1519/JSC.0b013e3181b94a7b> (2011).
48. Pitkin, M., Muppavarapu, R., Cassidy, C. & Pitkin, E. Subperiosteal transmission of intra-articular pressure between articulated and stationary joints. *Sci. Rep.* **5**, 8103. <https://doi.org/10.1038/srep08103> (2015).
49. Vilenky, J. Primate locomotion: Utilization and control of symmetrical gaits. *Annu. Rev. Anthropol.* **18**, 17–35. <https://doi.org/10.1146/annurev.anthro.18.1.17> (1989).
50. Desai, S. J. *et al.* An anthropometric study of the distal humerus. *J. Shoulder Elbow Surg.* **23**, 463–469. <https://doi.org/10.1016/j.jse.2013.11.026> (2014).
51. Sanz-Idirin, A., Arroyave-Tobon, S., Linares, J.-M. & Arrazola, P. J. Load bearing performance of mechanical joints inspired by elbow of quadrupedal mammals. *Bioinspir. Biomimetics* **16**, 046025. <https://doi.org/10.1088/1748-3190/abe57> (2021).
52. Gregersen, C. S., Silvertown, N. A. & Carrier, D. R. External work and potential for elastic storage at the limb joints of running dogs. *J. Exp. Biol.* **201**, 3197–3210. <https://doi.org/10.1242/jeb.201.23.3197> (1998).
53. Norberg, R. Å. & Aldrin, B. S. Scaling for stress similarity and distorted-shape similarity in bending and torsion under maximal muscle forces concurs with geometric similarity among different-sized animals. *J. Exp. Biol.* **213**, 2873–2888. <https://doi.org/10.1242/jeb.044180> (2010).
54. Coatham, S. J., Sellers, W. I. & Püschel, T. A. Convex hull estimation of mammalian body segment parameters. *R. Soc. Open Sci.* **8**, 210836. <https://doi.org/10.1098/rsos.210836> (2021).
55. Fedorov, A. *et al.* 3D Slicer as an image computing platform for the Quantitative Imaging Network. *Magn. Reson. Imaging* **30**, 1323–1341. <https://doi.org/10.1016/j.mri.2012.05.001> (2012).
56. Botton-Divet, L., Houssaye, A., Herrel, A., Fabre, A. C. & Cornette, R. Tools for quantitative form description; an evaluation of different software packages for semi-landmark analysis. *PeerJ* **1–18**, 2015. <https://doi.org/10.7717/peerj.1417> (2015).
57. Christiansen, P. Scaling of the limb long bones to body mass in terrestrial mammals. *J. Morphol.* **239**, 167–190. [https://doi.org/10.1002/\(SICI\)1097-4687\(199902\)239:2%3C167::AID-JMOR5%3E3.0.CO;2-8](https://doi.org/10.1002/(SICI)1097-4687(199902)239:2%3C167::AID-JMOR5%3E3.0.CO;2-8) (1999).
58. Kilbourne, B. M. & Hoffman, L. C. Scale effects between body size and limb design in quadrupedal mammals. *PLoS ONE* <https://doi.org/10.1371/journal.pone.0078392> (2013).
59. Michaud, M., Toussaint, S. L. D. & Gilissen, E. The impact of environmental factors on the evolution of brain size in carnivores. *Commun. Biol.* **5**, 998. <https://doi.org/10.1038/s42003-022-03748-4> (2022).
60. Labonte, D. *et al.* Extreme positive allometry of animal adhesive pads and the size limits of adhesion-based climbing. *Proc. Natl. Acad. Sci. U. S. A.* **113**, 1297–1302. <https://doi.org/10.1073/pnas.1519459113> (2016).
61. Upham, N. S., Esselstyn, J. A. & Jetz, W. Inferring the mammal tree: Species-level sets of phylogenies for questions in ecology, evolution, and conservation. *PLoS Biol.* **17**, e3000494. <https://doi.org/10.1371/journal.pbio.3000494> (2019).
62. Pagel, M. Inferring the historical patterns of biological evolution. *Nature* **401**, 877–884. <https://doi.org/10.1038/44766> (1999).
63. Revell, L. J. Phylogenetic signal and linear regression on species data. *Methods Ecol. Evol.* **1**, 319–329. <https://doi.org/10.1111/j.2041-210X.2010.00044.x> (2010).
64. Orme, D. *et al.* *caper: Comparative Analyses of Phylogenetics and Evolution in R* (2018). R package version 1.0.1.
65. R Core Team. *R: A Language and Environment for Statistical Computing*. R Foundation for Statistical Computing, Vienna, Austria (2022).
66. Revell, L. & Harmon, L. *Phylogenetic Comparative Methods in R* (Princeton University Press, 2022).
67. Warton, D. I., Wright, I. J., Falster, D. S. & Westoby, M. Bivariate line-fitting methods for allometry. *Biol. Rev.* **81**, 259. <https://doi.org/10.1017/S1464793106007007> (2006).
68. Warton, D. I., Duursma, R. A., Falster, D. S. & Taskinen, S. smatr 3- an R package for estimation and inference about allometric lines. *Methods Ecol. Evol.* **3**, 257–259. <https://doi.org/10.1111/j.2041-210X.2011.00153.x> (2012).

Acknowledgements

We thank Dr. Stephane Viollet (Aix-Marseille Univ., ISM) for proofreading the manuscript and for his helpful recommendations. This research was supported by the French Research National Agency (Agence Nationale de la Recherche, ANR) Grant No. ANR-20-CE10-0008, through the project BioDesign.

Author contributions

All authors contributed to the conception of the study. K.M.F. performed the data acquisition and analyses, wrote the main manuscript and supplementary, and prepared figures and tables with input from S.A.T. and L.T.; S.A.T., L.T., and J.M.L. provided analytical tools and technical advice. All authors revised and approved the manuscript.

Competing interests

The authors declare no competing interests.

Additional information

Supplementary Information The online version contains supplementary material available at <https://doi.org/10.1038/s41598-023-50619-x>.

Correspondence and requests for materials should be addressed to K.M.-F.

Reprints and permissions information is available at www.nature.com/reprints.

Publisher's note Springer Nature remains neutral with regard to jurisdictional claims in published maps and institutional affiliations.



Open Access This article is licensed under a Creative Commons Attribution 4.0 International License, which permits use, sharing, adaptation, distribution and reproduction in any medium or format, as long as you give appropriate credit to the original author(s) and the source, provide a link to the Creative Commons licence, and indicate if changes were made. The images or other third party material in this article are included in the article's Creative Commons licence, unless indicated otherwise in a credit line to the material. If material is not included in the article's Creative Commons licence and your intended use is not permitted by statutory regulation or exceeds the permitted use, you will need to obtain permission directly from the copyright holder. To view a copy of this licence, visit <http://creativecommons.org/licenses/by/4.0/>.

© The Author(s) 2024